The Role of Ocean–Atmosphere Coupling in the Zonal-Mean Atmospheric Response to Arctic Sea Ice Loss

CLARA DESER, ROBERT A. TOMAS, AND LANTAO SUN

National Center for Atmospheric Research, Boulder, Colorado*

(Manuscript received 30 April 2014, in final form 24 November 2014)

ABSTRACT

The role of ocean–atmosphere coupling in the zonal-mean climate response to projected late twenty-first-century Arctic sea ice loss is investigated using Community Climate System Model version 4 (CCSM4) at 1° spatial resolution. Parallel experiments with different ocean model configurations (full-depth, slab, and no interactive ocean) allow the roles of dynamical and thermodynamic ocean feedbacks to be isolated. In the absence of ocean coupling, the atmospheric response to Arctic sea ice loss is confined to north of 30°N, consisting of a weakening and equatorward shift of the westerlies accompanied by lower tropospheric warming and enhanced precipitation at high latitudes. With ocean feedbacks, the response expands to cover the whole globe and exhibits a high degree of equatorial symmetry: the entire troposphere warms, the global hydrological cycle strengthens, and the intertropical convergence zones shift equatorward. Ocean dynamics are fundamental to producing this equatorially symmetric pattern of response to Arctic sea ice loss. Finally, the absence of a poleward shift of the wintertime Northern Hemisphere westerlies in CCSM4's response to greenhouse gas radiative forcing is shown to result from the competing effects of Arctic sea ice loss and greenhouse warming on the meridional temperature gradient in middle latitudes.

1. Introduction

Perennial Arctic sea ice is projected to disappear by the mid-to-late twenty-first century in response to anthropogenically driven increases in greenhouse gas (GHG) concentrations (Stroeve et al. 2012; Stocker et al. 2013). The anticipated loss of Arctic sea ice is expected to impact climate at northern high and middle latitudes through a variety of mechanisms (e.g., Serreze and Barry 2011). The most robust impacts include thermodynamically driven warming and moistening of the polar atmosphere and adjacent high-latitude continents, and an associated weakening of the zonal-mean westerlies (e.g., Deser et al. 2010; Liu et al. 2012; Screen et al. 2013; Peings and Magnusdottir 2014). Less certain are impacts related to regional atmospheric circulation changes, such as cooling over portions of Eurasia and North America induced by high pressure systems (Liu et al. 2012; Screen et al. 2013) and an increase in extreme weather events associated with enhanced jet stream meanders (e.g., Francis and Vavrus 2012; Screen and Simmonds 2013; Barnes 2013).

The role of ocean–atmosphere coupling in the climate response to projected Arctic sea ice loss has received little attention. Two early modeling studies, Rind et al. (1995, hereafter R95) and Chiang and Bitz (2005, hereafter CB05), considered local thermodynamic air–sea interaction by coupling a 50-m "slab" ocean mixed layer model to an atmospheric general circulation model (AGCM). Study R95 prescribed global sea ice cover produced by the Goddard Institute for Space Sciences (GISS) model under present-day CO_2 levels as a boundary condition to the same model under doubled CO_2, thereby isolating the role of GHG-induced sea ice loss. CB05 specified an idealized pattern of sea ice expansion over the Northern Hemisphere (NH) relevant for understanding the Last Glacial Maximum (LGM) to the Community Climate Model version 3 (CCM3). Both studies found that local thermodynamic air–sea coupling allowed the atmospheric response to propagate into the tropics. In CB05, this tropical response took the form of a shift in the intertropical convergence zone (ITCZ)

* The National Center for Atmospheric Research is sponsored by the National Science Foundation.

Corresponding author address: Dr. Clara Deser, 1850 Table Mesa Drive, Climate and Global Dynamics Division, NCAR, Boulder CO 80307.
E-mail: cdeser@ucar.edu

DOI: 10.1175/JCLI-D-14-00325.1

away from the hemisphere with enhanced ice cover. R95 reported that the tropical troposphere warms and moistens in response to sea ice loss, but did not comment on the structure of the temperature and precipitation changes. We note that both studies used relatively coarse-resolution AGCMs by today's standards.

A more complete treatment of oceanic feedbacks was employed by Scinnoca et al. (2009) and Graversen and Wang (2009) through surface albedo modifications within a fully coupled modeling framework (e.g., atmosphere, full-depth ocean, sea ice, and land model components). Specifically, Scinocca et al. (2009) investigated the transient response of the Canadian Middle Atmosphere Model (CMAM) to a sudden reduction in sea ice albedo, while Graversen and Wang (2009) examined the equilibrium response of the Community Climate System Model version 3 (CCSM3) to a suppression of all surface albedo feedbacks (sea ice, snow cover, and terrestrial vegetation) in a doubled CO_2 experiment. Scinocca et al. (2009) focused on the stratospheric circulation and ozone responses in the Arctic, finding a strengthening of the polar vortex and a decrease in ozone concentration in spring in response to sea ice loss. Graversen and Wang (2009) emphasized the role of surface albedo feedbacks in polar amplification, finding that about one-third of the surface temperature response in the Arctic and approximately 15% of "Arctic amplification" (the ratio between Arctic and global temperature responses to doubled CO_2) results from these feedbacks. Neither study investigated the response of the tropospheric circulation in detail or isolated the role of ocean feedbacks (e.g., by comparison to atmosphere-only model experiments). Furthermore, as we shall show, the approaches of Scinocca et al. (2009) and Graversen and Wang (2009) consider only the effects of Arctic sea ice loss during the sunlit portion of the year (e.g., via shortwave radiative changes associated with lowered sea ice albedo). However, winter sea ice loss, although less pronounced than in other seasons, has a disproportionate impact on the annual mean net surface heat budget due to the added contribution of the turbulent energy fluxes which maximize in the cold season (Deser et al. 2010; Peings and Magnusdottir 2014). Thus, the full effect of year-round Arctic sea ice loss on the coupled climate system remains to be addressed.

Here we investigate the role of dynamic and thermodynamic ocean–atmosphere coupling in the global climate response to projected late twenty-first-century Arctic sea ice loss using Community Climate System Model version 4 (CCSM4) at 1° spatial resolution. Our experiments incorporate a realistic seasonal cycle of sea ice loss, enabling a more complete assessment of its role in future climate change than in previous studies. To explicitly isolate the contribution of ocean feedbacks, we conduct companion experiments using the atmospheric model component of CCSM4 with prescribed sea ice and SST. Additional simulations with the slab ocean version of CCSM4 provide further insight into the roles of dynamic versus thermodynamic ocean coupling in the response to Arctic sea ice loss. We focus our analysis on the vertical and latitudinal structures of the zonal-mean temperature and zonal wind responses. Additional results are provided for precipitation, SST, and northward energy transport responses.

The rest of this paper is organized as follows. Section 2 describes the model and design of the various experiments. Results are presented in section 3, starting with the net surface energy flux response (section 3a) followed by the zonal-mean temperature and zonal wind responses as a function of height and latitude (section 3b) in both the coupled and uncoupled Arctic sea ice loss experiments. Section 3c provides an assessment of the relative roles of Arctic sea ice loss and GHG increase in driving future changes in zonal winds over the extratropical Northern Hemisphere. Additional aspects of the response to Arctic sea ice loss are presented in the remainder of section 3, including the global hydrological cycle (section 3d), tropical precipitation and SST patterns (section 3e), and northward energy transport (section 3f). The paper concludes with a summary (section 4) and discussion (section 5) of the key results.

2. Model and experimental design

a. *CCSM4*

CCSM4 is a fully coupled ocean–atmosphere–land–cryosphere general circulation model, with an atmospheric component using a finite volume dynamical core at a horizontal resolution of 0.90° latitude and 1.25° longitude and 26 vertical levels and an oceanic resolution of 1.14° in longitude and variable in latitude (0.28° at the equator increasing to 0.66° at approximately 60°N) and 60 vertical levels (20 in the upper 200 m). The dynamic–thermodynamic sea ice model includes a subgrid-scale ice thickness distribution, energy-conserving thermodynamics, and elastic–viscous–plastic dynamics (Holland et al. 2012). Details of the model components and their coupling may be found in Gent et al. (2011) and references therein. CCSM4 simulates well the observed late twentieth-century distributions of Arctic sea ice concentration and thickness, as well as trends over the past few decades (Kay et al. 2011; Jahn et al. 2012; Wettstein and Deser 2014). Other aspects of the model's climatology and variability are presented in the CCSM4

TABLE 1. Details of the model experiments. For reference, ΔICE_coupled = ICE_coupled_21 − ICE_coupled_20; ΔICE_coupled_albedo = ICE_coupled_albedo_21 − ICE_coupled_20; ΔICE_atm = ICE_atm_21 − ICE_atm_20; and ΔRCP8.5 = RCP8.5 − Historical.

Name	Model configuration	Radiative forcing	Arctic sea ice target/ forcing	Years of simulation
ICE_coupled_20	CCSM4	Year 2000	1980–99/longwave	360
ICE_coupled_21	CCSM4	Year 2000	2080–99/longwave	360
ICE_coupled_albedo_21	CCSM4	Year 2000	2080–99/modified albedo	100
ICE_atm_20	CAM4	Year 2000	2080–99/prescribed	260
ICE_atm_21	CAM4	Year 2000	2080–99/prescribed	260
Historical	CCSM4	Variable	1980–99	6 runs
RCP8.5	CCSM4	Variable	2080–99	6 runs

special issue collection of the *Journal of Climate* (2012). This version of CCSM4 contributed to the Coupled Model Intercomparison Project phase 5 (CMIP5; Taylor et al. 2012). We also make use of the slab-ocean model (SOM) configuration of CCSM4, here termed CCSM4_som. In this configuration, the full-depth ocean model with active dynamics is replaced with a slab mixed layer ocean model with spatially and seasonally varying mixed layer depths; all other model components (including sea ice) are identical to those in CCSM4 (Bitz et al. 2012). The mean effects of ocean heat transport on the SST are represented by specifying a climatological monthly Q_{flux} to the CCSM4_som. Details of the Q_{flux} and mixed layer depth specification are provided in section 2b.

b. Coupled model experiments with constrained sea ice

In the coupled model experiments, we artificially control the seasonal cycle of Arctic sea ice concentration and thickness to approximate those in the ensemble mean of the six CCSM4 historical runs averaged over the period 1980–99, and those in the ensemble mean of the six CCSM4 RCP8.5 runs averaged over the period 2080–99. These constrained sea ice coupled model experiments are denoted ICE_coupled_20 and ICE_coupled_21 for the late twentieth- and late twenty-first-century sea ice states, respectively. In both experiments, radiative forcing conditions are kept fixed at the year 2000 in order to isolate the response to sea ice loss obtained upon differencing the two experiments. Both coupled experiments start from the 1 January 1990 state from an arbitrarily chosen CCSM4 historical run. To achieve the desired seasonal cycles of sea ice concentration and thickness for the late twentieth and twenty-first centuries, we specify an additional longwave radiative flux (LRF) to the ice model at each grid box and time step. We emphasize that this flux is prescribed only to the ice model and therefore only where and when there is sea ice. The LRF is seasonally dependent but for simplicity does not vary spatially, and is determined using an iterative procedure (see the appendix for details). In a given grid cell, we apply an annual-mean globally equivalent value of $0.10\,\text{W m}^{-2}$ upward LRF to simulate late twentieth-century sea ice conditions, and $0.43\,\text{W m}^{-2}$ downward LRF to simulate the late twenty-first-century sea ice conditions, with larger (smaller) values during months of thicker (thinner) ice cover. (Note that in order to simulate the late twentieth-century sea ice, a small upward LRF is needed to balance the additional ice melt that would have occurred if the historical run were run forward and the committed warming realized.) The LRF difference between the two runs is equivalent to an annual-mean globally averaged value of $0.54\,\text{W m}^{-2}$, which is 8% of the total radiative forcing in the representative concentration pathway 8.5 (RCP8.5) scenario between 2000 and 2100 ($6.7\,\text{W m}^{-2}$). The local monthly values of the applied LRF in each experiment are given in the table in the appendix. Note that by applying the LRF needed to keep the sea ice near a fixed concentration throughout the experiments, we effectively limit the amplitude of internally generated sea ice variability (not shown). The ICE_coupled_20 and ICE_coupled_21 experiments are each run for 360 years. Our analyses are based on averages over years 101–360 to avoid the initial transient adjustment of the Atlantic meridional overturning circulation (AMOC) to the sudden loss of Arctic sea ice in ICE_coupled_21 (not shown).

In the rest of this paper, we shall refer to the difference between ICE_coupled_21 and ICE_coupled_20 as ΔICE_coupled. Similarly, we refer to the difference between the period 2080–99 in the RCP8.5 runs and the period 1980–99 in the historical runs as ΔRCP8.5. The former isolates the coupled response of CCSM4 to GHG-induced Arctic sea ice loss, while the latter includes all feedbacks involved in CCSM4's response to GHG forcing. The statistical significance of the responses is assessed using a two-sided Student's t test. All of the experiments are summarized in Table 1.

We shall also make use of a similar set of constrained sea ice experiments with CCSM4_som, which are identical in design to those described above for CCSM4 except for the ocean model configuration. These experiments are denoted ICE_som_20 and ICE_som_21 for the late twentieth- and late twenty-first-century sea ice states, respectively. Spatially and seasonally varying

mixed layer depths in both experiments are taken from the monthly mean climatology of the ICE_coupled_20 experiment. Each CCSM4_som experiment is run for 300 years under radiative conditions fixed at the year 2000, and initialized from the same 1 January 1990 state as the CCSM4_coupled runs. The same LRF values are applied to the sea ice model in ICE_som_20 (ICE_som_21) as in ICE_coupled_20 (ICE_coupled_21). The same Q_{flux} is used in both CCSM4_som runs and is based on the climatological monthly SST distribution in ICE_coupled_20 (note that the Q_{flux} varies over the course of the seasonal cycle but is fixed from year to year). Thus, any changes in SSTs between ICE_som_20 and ICE_som_21 are due to thermodynamic processes alone. The difference between ICE_som_21 and ICE_som_20 is referred to as ΔICE_som, and is based on averages over years 41–300 to avoid the transient adjustment to the sudden loss of Arctic sea ice in ICE_som_21 (Table 1).

c. *Coupled model experiments with modified sea ice albedo*

In addition to the CCSM4 experiments with constrained Arctic sea ice, we have conducted a modified sea ice–albedo experiment with CCSM4 following the approach of Scinocca et al. (2009) and Graversen and Wang (2009). In particular, we lowered the sea ice albedo in the model's shortwave radiation formulation (Briegleb and Light 2007) to achieve a nearly ice-free September similar to that in the CCSM4 RCP8.5 simulation at the end of the twenty-first century (L. Landrum 2014, personal communication). Like our constrained sea ice experiments, the radiative forcing conditions for this experiment (hereafter referred to as ICE_coupled_albedo_21) are kept fixed at the year 2000 so as to isolate the effect of the sea ice loss. Similarly, ICE_coupled_albedo_21 is initialized with the 1 January 1990 state from a CCSM4 historical run. The modified sea ice albedo experiment was run for 100 years (note that the sea ice fully responds within a year or two of the albedo change). The difference between ICE_coupled_albedo_21 and ICE_coupled_20 is denoted ΔICE_coupled_albedo (Table 1). We limit our discussion of the results from ΔICE_coupled_albedo to the seasonal cycle of the simulated sea ice loss and corresponding net surface heat flux response; the length of the modified ice albedo run is sufficient for this purpose.

d. *Atmospheric model experiments with prescribed sea ice*

We have conducted a companion set of experiments with CAM4, the atmospheric model component of CCSM4, in which repeating seasonal cycles of ice concentration and thickness taken from CCSM4 are prescribed (see Table 1). In ICE_atm_20, the prescribed repeating sea ice seasonal cycle (in both hemispheres) is formed by averaging over the period 1980–99; in ICE_atm_21, it is formed by averaging over the period 2080–99 in the Arctic only (Antarctic sea ice is kept fixed at 1980–99 values). The sea ice conditions for 1980–99 (2080–99) are taken from the average of a six-member ensemble of historical (RCP8.5) runs with CCSM4. A similar approach was used in Deser et al. (2010) based on CCSM3. In ICE_atm_21, we also specify the accompanying 2080–99 SST conditions from CCSM4 at grid cells where the ice concentration in the late twenty-first century is lower than that in the late twentieth century. This approach accounts for the local ocean warming that is largely a by-product of the ice loss (see Screen et al. 2013, 2015). Elsewhere, SSTs are set to the 1980–99 CCSM4 values in both experiments. Each experiment is run for 260 yr, and our results are based on the average of years 1–260. The difference between ICE_atm_21 and ICE_atm_20, denoted ΔICE_atm, isolates the direct atmospheric response to GHG-induced Arctic sea ice loss in the absence of nonlocal oceanic feedbacks.

3. Results

a. *Arctic SIC and net surface heat flux response*

In response to RCP8.5 radiative forcing, CCSM4 shows a year-round reduction in Arctic sea ice extent (SIE; defined as the area with at least 15% fractional ice cover), manifest as a poleward contraction of the ice cover in the late twenty-first century compared to the late twentieth century (Fig. 1). In March, the month of greatest SIE, the ice loss occurs primarily within the marginal seas of the Pacific and Atlantic; in September, the month of least extensive ice, the reduction is confined to the central Arctic Ocean. By the late twenty-first century, the Arctic is projected to become essentially ice-free in late summer and early autumn (August–October) according to CCSM4 (Fig. 1).

The seasonal cycles of SIE in ICE_coupled_20 and ICE_coupled_21 show good agreement with their CCSM4 targets, except for a slight underestimate of the late twenty-first-century values in winter (Fig. 1). Correspondingly, the seasonal cycle of SIE loss (twenty-first minus twentieth century) in ΔICE_coupled is within 5% of that in ΔRCP8.5 during April–November, and 20%–25% less than ΔRCP8.5 during December–March (Fig. 2a). In contrast, ΔICE_coupled_albedo underestimates the SIE loss in ΔRCP8.5 by 65%–70% in December–March, 50% in November and April, and 10% in late summer (August–September). The maximum ice loss in ΔICE_coupled (-7×10^6 km^2 or 80% of the late twentieth-century mean) occurs in October–November,

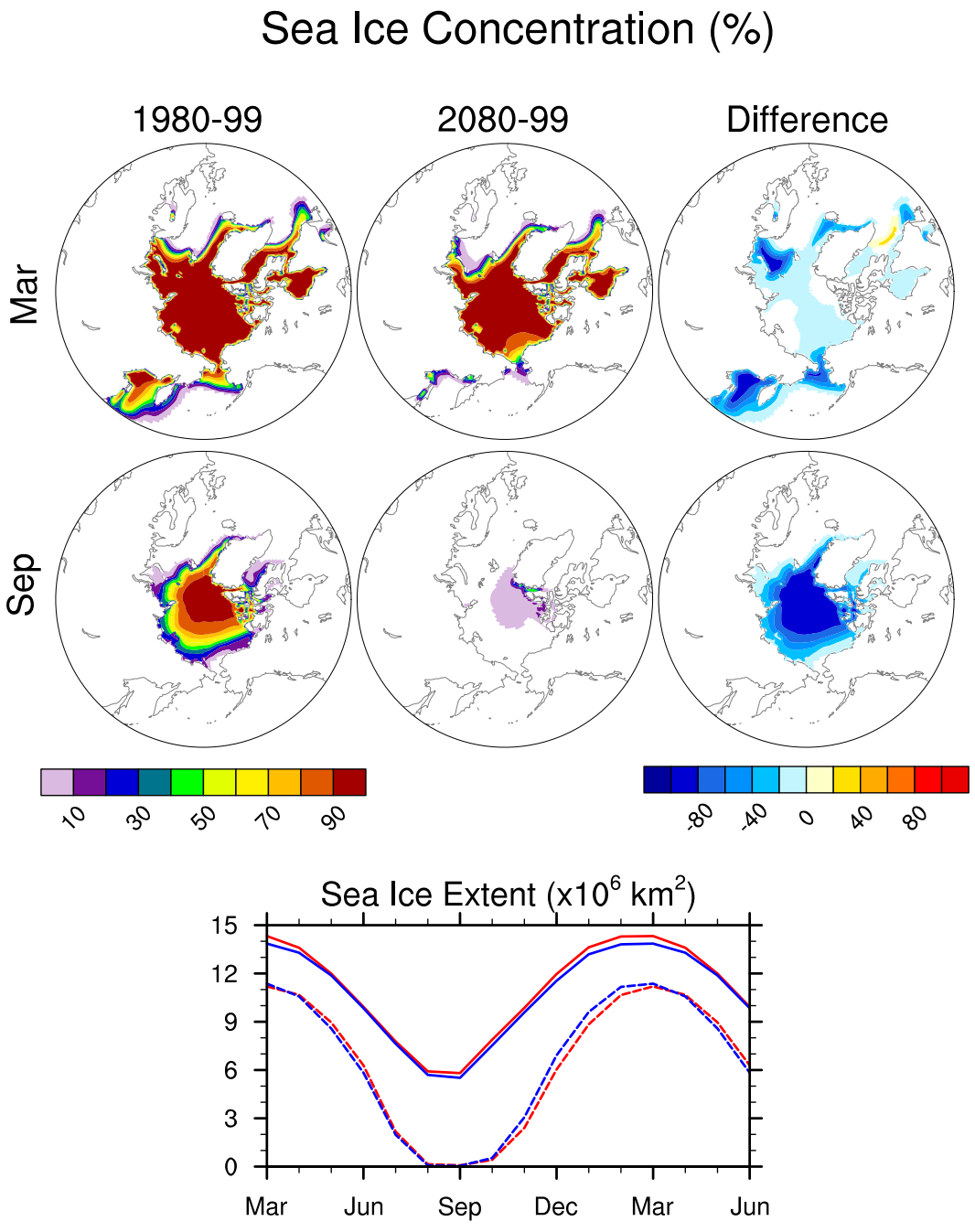

FIG. 1. Sea ice concentration (%) distributions in (top) March and (middle) September from the late (left) twentieth-century and (center) late twenty-first-century coupled experiments and (right) their difference. (bottom) Monthly Arctic sea ice extent (10^6 km^2) during the late twentieth century (solid lines) and late twenty-first century (dashed lines) from the historical and RCP8.5 CCSM4 experiments (red) and the Arctic sea ice coupled experiments (blue).

and the minimum ice loss occurs in February–April (-2.5×10^6 km^2 corresponding to a 20% reduction from the late twentieth century).

The local SST increase associated with Arctic sea ice loss, determined by averaging SSTs for all grid cells experiencing SIC loss in the late twenty-first century compared to the late twentieth century, shows maximum values in July–September (~2°C in ΔRCP8.5 and ~1.75°C in ΔICE_coupled) and minimum values in January–April (~0.8°C in ΔRCP8.5 and ~0.4°C in

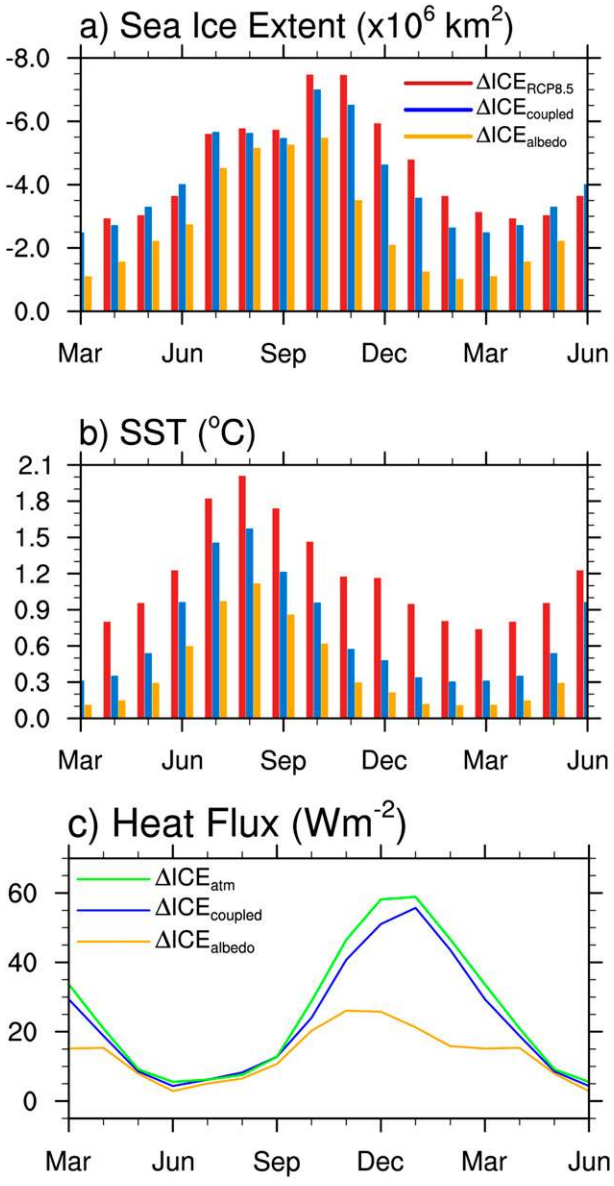

FIG. 2. (a) Late twenty-first-century minus late twentieth-century monthly Arctic sea ice extent (10^6 km^2; note inverted scale) from historical and RCP8.5 CCSM4 experiments (red), the coupled experiments (ΔICE_coupled; blue), and the albedo experiment (ΔICE_coupled_albedo; orange). The months March–June are repeated for clarity. (b) As in (a), but for SST (° C) averaged over all grid boxes in which the sea ice concentration is reduced in the late twenty-first century relative to the late twentieth century. (c) Net surface heat flux response (sum of the turbulent and longwave radiative flux components; W m^{-2}) to Arctic sea ice loss in ΔICE_coupled (blue), ΔICE_atm (green), and ΔICE_coupled_albedo (orange). See text for details.

ΔICE_coupled). The local Arctic Ocean SST increases in ΔICE_coupled_albedo are smaller than those in ICE_coupled (~20% less in summer and ~50% less in winter), likely due to the underestimated sea ice loss (Fig. 2b).

Arctic sea ice loss results in a net upward flux of energy from the ocean to the atmosphere as cold sea ice is replaced by (warmer) open water, with much greater heat content (Fig. 2c). This net upward surface heat flux is primarily in the form of turbulent sensible and latent energy fluxes, with a smaller contribution from longwave radiative fluxes [not shown, but see similar results in Deser et al. (2010)]. Note that the surface shortwave radiative flux does not affect the atmosphere directly, although it plays an important role in promoting sea ice melt by warming the upper ocean mixed layer. The largest net upward surface heat flux response occurs in December–January in both ΔICE_coupled and ΔICE_atm, despite the fact that the greatest ice loss occurs in October–November (Fig. 2c). As discussed in Deser et al. (2010) (see also Screen and Simmonds 2010), this delay results from the fact that the climatological air–sea temperature difference over the Arctic Ocean is greatest in winter, leveraging the efficiency of the turbulent energy fluxes.

The seasonal cycle of the net surface heat flux response is similar in ΔICE_coupled and ΔICE_atm, with maximum values ~50–60 W m^{-2} in December–January and minimum values of ~5 W m^{-2} in June–July (Fig. 3c). The wintertime heat flux response is ~(10%–15%) lower in the coupled experiment than the uncoupled experiment due mainly to the smaller magnitude of the ice loss and local SST warming. In contrast, the maximum net surface heat flux response in ΔICE_coupled_albedo is only 25 W m^{-2}, occurring in November–December. Averaged over the year, the net upward surface heat flux response in the Arctic is 25.3 W m^{-2} in ΔICE_coupled, 27.9 W m^{-2} in ΔICE_atm, and 14.4 W m^{-2} in ΔICE_coupled_albedo: thus, ΔICE_coupled_albedo underestimates the heat flux response in ΔICE_coupled and ΔICE_atm by 52% and 57%, respectively. This shows that the underestimate of winter ice loss in ΔICE_coupled_albedo has a disproportionate effect on the net annual surface heat flux response over the Arctic Ocean, and demonstrates the advantage of the longwave radiation–based approach for modifying sea ice compared to the traditional ice–albedo method.

In summary, the net upward surface heat flux response to late twenty-first-century Arctic sea ice loss maximizes in winter despite that the ice loss itself peaks in autumn. The shortwave effect of Arctic sea ice loss, through the positive ice–albedo feedback mechanism, accounts for only about half of the net surface heat flux response in winter and in the annual mean. This is due to the fact that processes other than the ice–albedo feedback mechanism contribute to the winter ice loss. This result has strong implications for the design of coupled experiments aimed at testing the role of sea ice loss in the

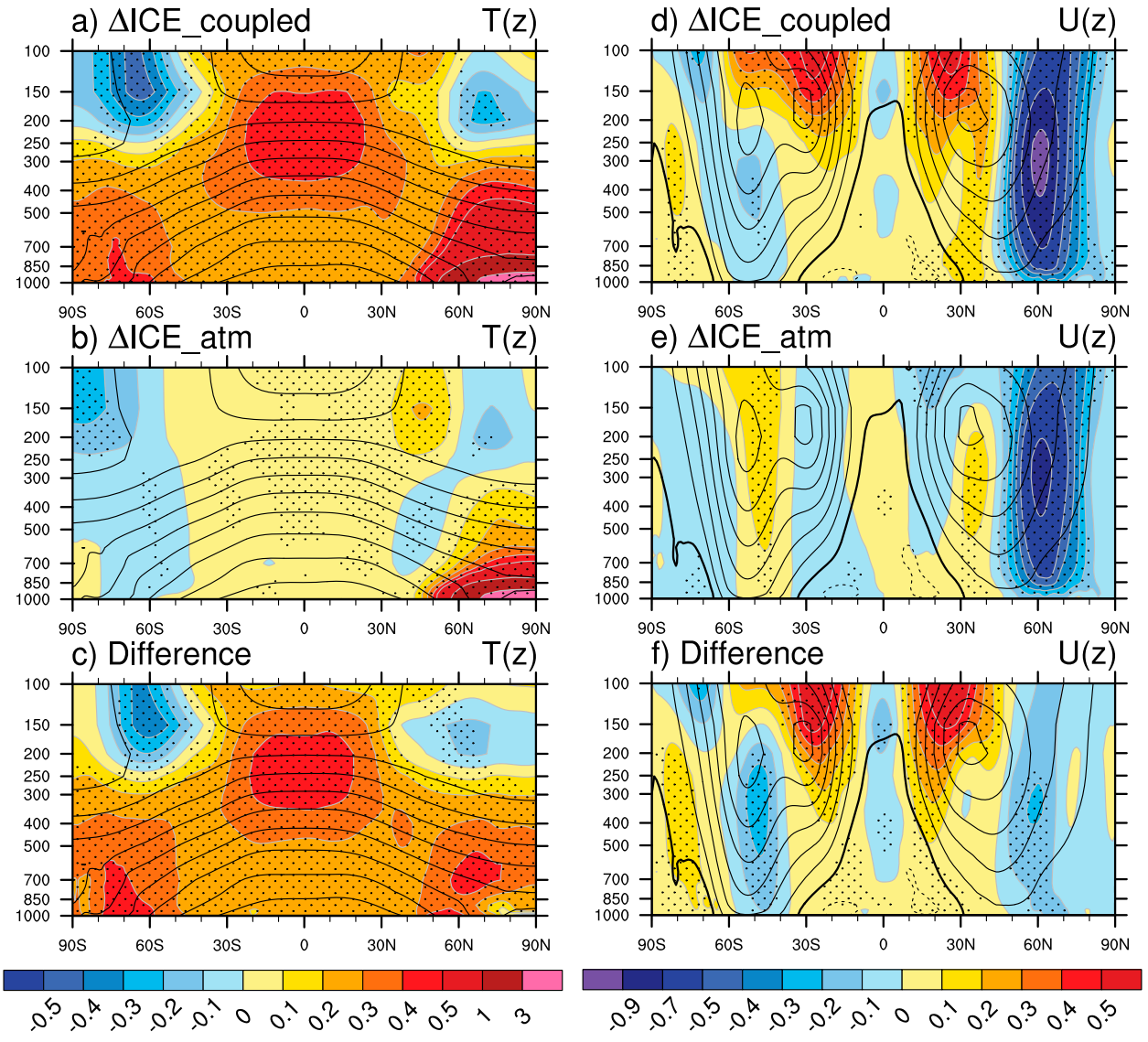

FIG. 3. Annual zonally averaged (a)–(c) air temperature (°C) and (d)–(f) zonal wind ($m\,s^{-1}$) responses (color shading; color bars at bottom of each column) to Arctic sea ice loss in (top)–(bottom) ΔICE_coupled, ΔICE_atm, and their difference. Stippling indicates that the response is statistically significant at the 95% confidence level. Contours indicate the climatological temperature (contour interval of 10°C) and zonal wind (contour interval of 5 $m\,s^{-1}$, zero contour thickened) distributions from the control runs.

climate system. Next, we investigate the global temperature and zonal wind responses to Arctic sea ice loss, which are initiated by the anomalous upward surface heat fluxes in regions of ice melt.

b. *Zonal-mean temperature and zonal wind responses to Arctic sea ice loss*

The zonally averaged annual-mean temperature and zonal wind responses as a function of height and latitude from the coupled and uncoupled experiments are shown in Fig. 3, superimposed upon the climatological distributions from the corresponding control (e.g., late twentieth century) runs. The thermal response in ΔICE_coupled is global in extent and exhibits remarkable symmetry about the equator, even though the forcing is confined to the surface of the Arctic Ocean (Fig. 3a). The entire troposphere warms by a few tenths of °C, with relative maxima in the tropical upper troposphere (0.5°C) and near the surface at both poles (0.5°C at 60°–80°S and 6°C at 80°–90°N). In addition to tropospheric warming, the extratropical lower stratosphere in both hemispheres cools slightly. This pattern bears a strong resemblance to the fully coupled climate response to increased GHG (ΔRCP8.5) as discussed below, albeit with reduced amplitude (~10% in most areas outside of the Arctic; Table 2).

TABLE 2. Selected regional zonal-mean responses to twenty-first-century Arctic sea ice loss in ΔICE_coupled ΔICE_atm and ΔRCP8.5: (top) annual mean and (bottom) DJF. SAT_{Arctic}: 2-m air temperature (°C) averaged over 65°–90°N; P_{Arctic}: precipitation (mm day^{-1}) averaged over 65°–90°N; U_{65N}: 700-hPa zonal wind (m s^{-1}) at 65°N; SAT_{Global}: globally averaged 2-m air temperature (°C); $[T]_{Global}$: 1000–300-hPa global temperature average (°C); $P_{15n\text{-}15s}$: precipitation (mm day^{-1}) averaged over 15°S–15°N; and $[T_U]_{tropics}$: upper tropical tropospheric temperature (500–100 hPa, 15°S–15°N) average (°C). Percentages are with respect to the values in ΔRCP8.5.

ANN	SAT_{Arctic}	P_{Arctic}	U_{65n}	SAT_{Global}	$[T]_{Global}$	$P_{15n\text{-}15s}$	$[T_U]_{tropics}$
ΔICE_coupled	5.76	0.14	−0.68	0.64	0.36	0.04	0.36
	74%	41%	—	17%	9%	15%	8%
ΔICE_atm	5.44	0.12	−0.57	0.35	0.07	0.00	0.02
	69%	35%	—	10%	2%	0%	0%
ΔRCP8.5	7.83	0.34	0.11	3.66	3.95	0.27	4.74
DJF	SAT_{Arctic}	P_{Arctic}	U_{65n}	SAT_{Global}	$[T]_{Global}$	$P_{15n\text{-}15s}$	$[T_U]_{tropics}$
ΔICE_coupled	9.67	0.19	−1.35	0.89	0.40	0.04	0.36
	88%	56%	—	24%	10%	14%	8%
ΔICE_atm	9.14	0.16	−0.99	0.62	0.11	0.01	0.02
	83%	47%	—	17%	3%	3%	0%
ΔRCP8.5	11.01	0.34	−0.42	3.75	3.90	0.29	4.74

Unlike the coupled run, the thermal response in ΔICE_atm is mainly confined to the extratropical Northern Hemisphere (Fig. 3b). Further, the Arctic warming is considerably shallower in ΔICE_atm compared to ΔICE_coupled (the 0.5°C contour reaches 700 versus 400 hPa), and does not extend as far south (the 0.5°C contour reaches 50° versus 40°N). However, the magnitude of Arctic surface warming (~5.8° versus 5.4°C) is similar between the two runs (Table 2). The role of air–sea interaction in the response to projected Arctic sea ice loss is obtained by subtracting ΔICE_atm from ΔICE_coupled (Fig. 3c). Ocean–atmosphere feedback imparts a high degree of equatorial symmetry to the thermal response; notably, the magnitude and vertical structure of the temperature increase at high latitudes is comparable between the hemispheres.

Consistent with the thermal response, the zonally averaged zonal wind response to Arctic sea ice loss in ΔICE_coupled exhibits a weakening of the westerlies on their poleward flank (45°–75°N), with maximum amplitudes of ~1 m s^{-1} at 60°N and 350 hPa, and a more modest strengthening of the westerlies in the core of the jet at upper levels and on their equatorward side at lower levels (30°–40°N; Fig. 3d). This statistically significant pattern resembles the negative phase of the northern annular mode (NAM). In addition to the northern extratropics, the tropical lower stratosphere shows an equatorially symmetric and statistically significant response of strengthened westerlies on the equatorward side of the jet maxima, with peak values ~0.5 m s^{-1} in both hemispheres. The extratropical Southern Hemisphere shows a weak but statistically significant tropospheric zonal wind response, with positive values near the pole and negative values at middle latitudes indicative of a weakening of the jet.

Like ΔICE_coupled, ΔICE_atm shows a significant negative NAM response but the amplitude is ~30% weaker in the middle and upper troposphere, consistent with the difference in vertical extent of the tropospheric warming (Fig. 3e). Elsewhere, the uncoupled zonal wind response is weak, but interestingly of opposite sign to that in the coupled run. The band of enhanced westerlies ~(40°–50°S) is significant throughout the depth of the troposphere and lower stratosphere. Subtracting the coupled and uncoupled responses reveals a high degree of equatorial symmetry throughout the troposphere and lower stratosphere, in keeping with the structure of the thermal response induced by ocean feedbacks (Fig. 3f). However, the configuration of the zonal wind response relative to the zonal wind climatology is different in the two hemispheres, due in part to the presence of two distinct jets in the SH and only one in the NH in the annual mean.

The zonally averaged temperature and zonal wind responses in December–February (DJF), the season of maximum Arctic Ocean heat flux response, are shown in Fig. 4. The global structure of the response is similar between boreal winter and the annual mean, but the amplitudes are larger especially in the NH extratropics. For example, the warming of the Arctic planetary boundary layer and free troposphere in ΔICE_coupled is approximately 70% greater and extends ~10° latitude farther south in DJF compared to the annual mean (Fig. 4a and Table 2). Similarly, ΔICE_atm shows stronger near-surface Arctic warming in winter than in the annual mean (Fig. 3b). In the Antarctic, the main difference between the ΔICE_coupled temperature responses in DJF and the annual mean is the lack of surface-intensified warming in the band 60°–80°S, consistent with the absence of sea ice in this region in austral

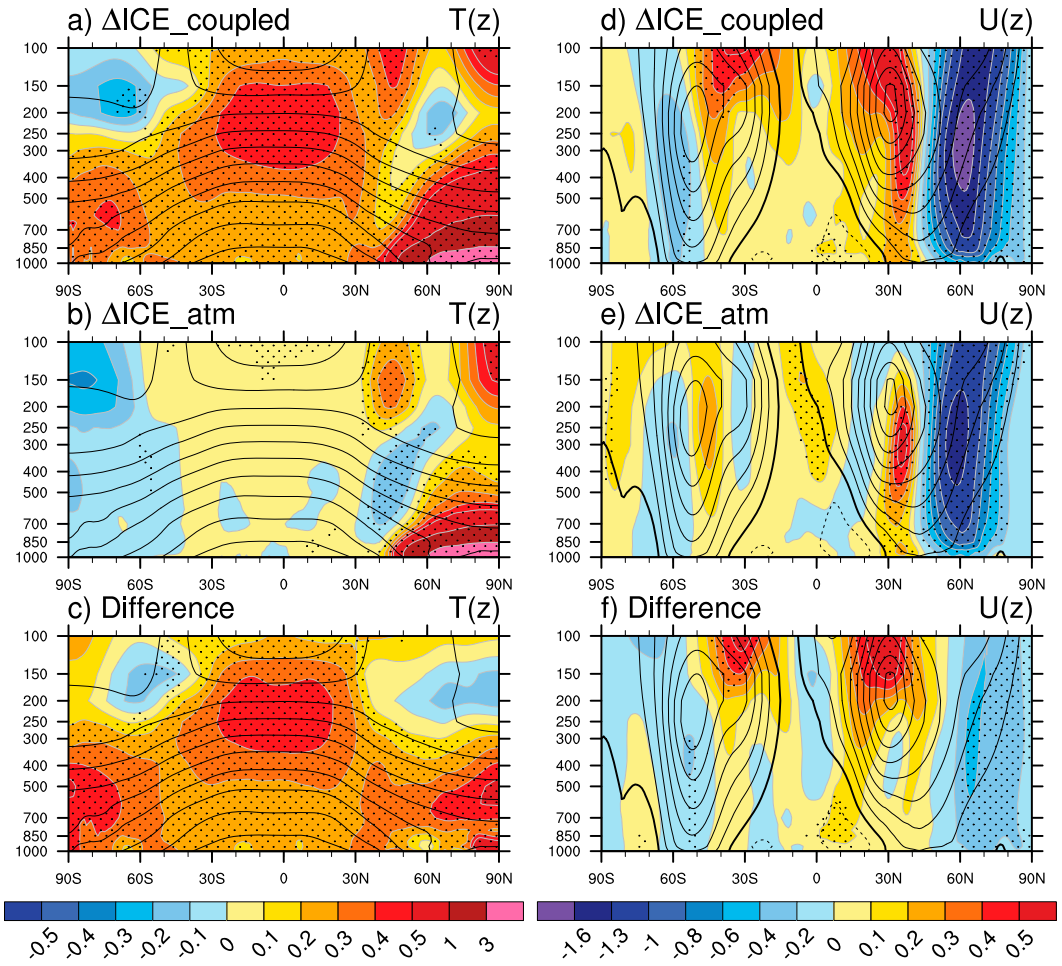

FIG. 4. As in Fig. 3, but for December–February averages. Note the different $U(z)$ color scale compared to Fig. 3.

summer (Fig. 4b). Subtracting the coupled and uncoupled thermal responses in DJF reveals a similar global structure as that in the annual mean, with ~30% larger magnitudes in the free troposphere at high latitudes (Fig. 4c).

Zonal wind in ΔICE_coupled shows a significant negative NAM response that is approximately twice as strong in DJF than in the annual mean, with maximum easterly (westerly) wind anomalies ~2 m s^{-1} at 60°N (~0.75 m s^{-1} at 35°N) in the upper troposphere (Fig. 4d; note the different color scale compared to Fig. 3d). In the SH, the DJF zonal wind response in ΔICE_coupled resembles the negative phase of the southern annular mode (SAM), with negative anomalies on the poleward side of the jet and positive anomalies on the equatorward flank; however, only the negative anomalies are significant. Thus, relative to the climatological jet position, the extratropical zonal wind responses in DJF in ΔICE_coupled are analogous between the two hemispheres. The DJF extratropical zonal wind responses in ΔICE_atm are similar in structure but weaker in magnitude compared to those in ΔICE_coupled, and only the NH anomalies are significant (Fig. 4e). The main impact of atmosphere–ocean coupling in DJF is to significantly enhance the strength of the easterly wind response at northern high latitudes by ~35% (Fig. 4f and Table 2).

c. *Role of Arctic sea ice loss in GHG-forced temperature and zonal wind responses*

We can estimate the role of Arctic sea ice loss in CCSM4's response to RCP8.5 radiative forcing at the end of the twenty-first century by comparing ΔRPC8.5 and ΔICE_coupled. It is worth clarifying that although it takes approximately a century for the AMOC to adjust to the sudden reduction of Arctic sea ice in ICE_coupled_21, the atmosphere adjusts much more rapidly (within 20 yr; not shown). Furthermore, the gradual loss of Arctic sea ice over the course of the twenty-first century in the RCP8.5 simulation allows the atmosphere to remain in

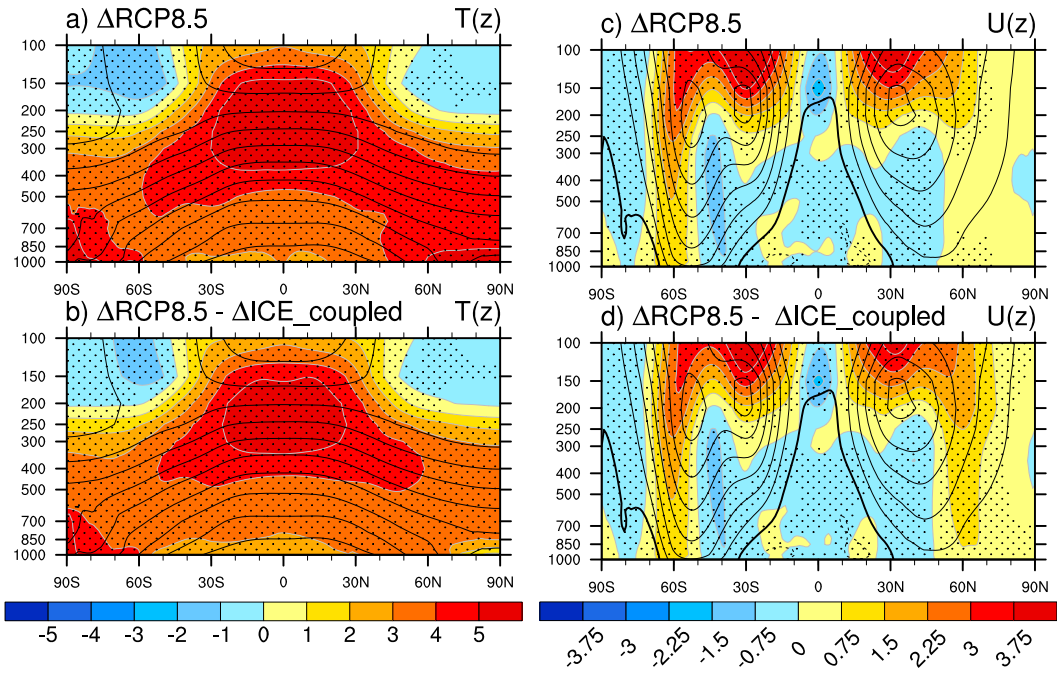

FIG. 5. Annual zonally averaged (a) air temperature (°C) and (c) zonal wind (m s^{-1}) responses (color shading) in ΔRCP8.5; (b),(d) as in (a),(c), but after removing the effects of Arctic sea ice loss (obtained by subtracting ΔICE_coupled from ΔRCP8.5). Stippling indicates that the response is statistically significant at the 95% confidence level. Contours as in Fig. 3.

quasi-equilibrium with the sea ice in any given decade. These considerations justify the comparison of the atmospheric responses in ΔRPC8.5 and ΔICE_coupled.

The thermal response ΔRPC8.5 shows the canonical structure of tropospheric warming and lower stratospheric cooling, with amplified temperature increases in the tropical upper troposphere. In addition to this equatorially symmetric pattern, ΔRPC8.5 exhibits stronger tropospheric warming in the extratropics of the NH compared to the SH (Fig. 5a). The accompanying zonal wind response is largely symmetric with respect to the equator at low latitudes, but shows substantial differences between the hemispheres at high latitudes (Fig. 5c). In particular, the NH lacks any appreciable tropospheric zonal wind signal poleward of ~50°N, whereas the SH shows strong positive zonal wind anomalies on the poleward flank of the midlatitude jet and negative anomalies to the south. Subtracting ΔICE_coupled from ΔRPC8.5 reveals that Arctic sea ice loss is responsible for most of the deviation from equatorial symmetry in the temperature and zonal wind responses to GHG forcing (Figs. 5b,d). In particular, the enhanced warming of the extratropical troposphere in the NH compared to the SH is eliminated after the effects of Arctic sea ice loss are removed. In addition, the zonal wind responses in the two hemispheres are brought into better alignment, with consistent poleward shifts of the midlatitude westerly jets in both hemispheres after accounting for the effects of Arctic sea ice loss (Fig. 5d). The only remaining hemispheric asymmetry in the zonal wind response in Fig. 5d occurs near the poles, with a significant easterly response in the SH and negligible response in the NH.

The seasonal evolution of the 700-hPa zonal mean zonal wind response in ΔRPC8.5 is shown in Fig. 6a. While the SH shows a consistent poleward shift of the midlatitude westerlies throughout the year in response to RCP8.5 radiative forcing, the analogous poleward shift in the NH is only present and significant during the warm half of the year. After subtracting the effects of Arctic sea ice loss (e.g., ΔRPC8.5 − ΔICE_coupled), the NH shows a continuous and significant poleward shift of the westerlies throughout the year, bringing the two hemispheres into better alignment (Fig. 6b). This striking result demonstrates that the lack of a poleward shift of the wintertime midlatitude eddy-driven jet in response to RCP8.5 radiative forcing is due to the opposing effects of Arctic sea ice loss and GHG increase in CCSM4. Similar results are found for averages over the Pacific and Atlantic basins separately (not shown).

d. Zonal-mean atmospheric condensational heating and precipitation responses to Arctic sea ice loss

A striking aspect of the coupled climate response to Arctic sea ice loss is the global extent of the tropospheric warming, with relative maxima at upper levels in the tropics and in the lower troposphere at high latitudes,

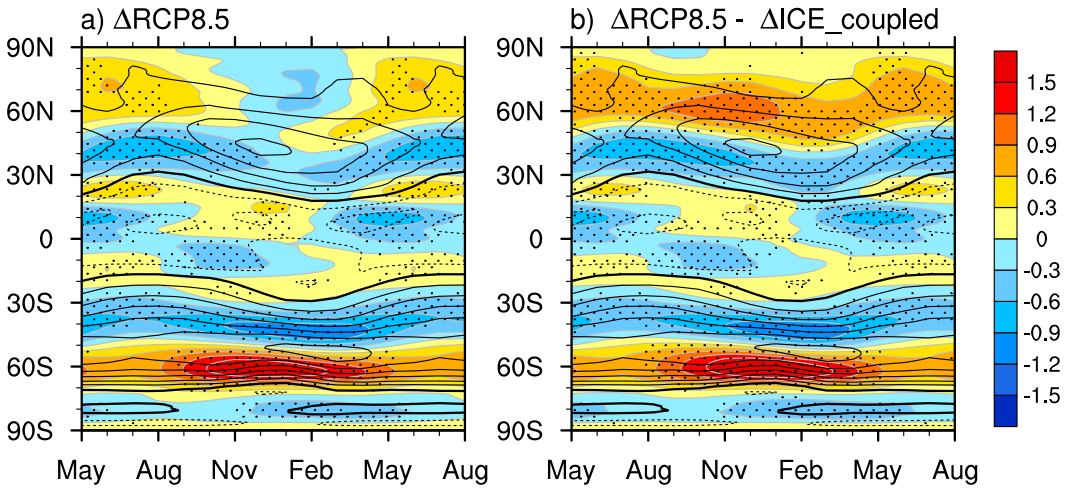

FIG. 6. (a) Monthly zonally averaged 700-hPa zonal wind ($m\,s^{-1}$) response (color shading) in ΔRCP8.5; (b) as in (a), but after removing the effects of Arctic sea ice loss (obtained by subtracting ΔICE_coupled from ΔRCP8.5). Stippling indicates that the response is statistically significant at the 95% confidence level. Contours indicate the climatological values from the CCSM4 historical run (contour interval is $5\,m\,s^{-1}$, zero contour is thickened, and negative values are dashed). The months May–August have been repeated for clarity.

a pattern that resembles the GHG-forced response (recall Fig. 5a). This warming pattern is accompanied by an intensification of the global atmospheric hydrological cycle as shown in Fig. 7. In particular, atmospheric condensational heating in ΔICE_coupled increases in the upper troposphere and decreases in the lower troposphere, indicative of an upward and poleward shift of the climatological heating maxima in both hemispheres (Fig. 7a). Embedded within this large-scale pattern is an intensification of the two ITCZ heating maxima, especially on their equatorward sides near 5°N and 5°S. The Arctic planetary boundary layer also shows an increase in condensational heating. The global structure of the condensational heating response to Arctic sea ice loss bears a striking resemblance to that in ΔRPC8.5, with ~15% of the amplitude, reinforcing the notion that Arctic sea ice loss leads to a "mini" global warming pattern when ocean feedbacks are included (Fig. 7b; note different color scale). In contrast, without ocean feedbacks, the condensational heating response to Arctic sea ice loss is primarily confined to the Arctic planetary boundary layer (not shown).

Consistent with the atmospheric condensational heating response, ΔICE_coupled shows a global increase in precipitation, with the largest increases in the Arctic (~0.2 mm day^{-1}), and more modest increases in the deep tropics (~0.05–0.10 mm day^{-1}) and middle latitudes of both hemispheres (~0.05 mm day^{-1}) (blue curve in Fig. 7c, left *y*-axis scale). Most of the precipitation increase poleward of ~70°N is due to the direct atmospheric response to sea ice loss (ΔICE_atm; green curve in Fig. 7c, left *y*-axis scale), while the nonlocal precipitation enhancement is due to ocean–atmosphere coupling. Thus, air–sea feedbacks impart a high degree of equatorial symmetry to the global-scale precipitation response (dotted blue curve in Fig. 7c, left *y*-axis scale), a structure that resembles the fully coupled response to GHG forcing (ΔRPC8.5) with ~15% of the amplitude (red curve in Fig. 7c, right *y*-axis scale).

e. *Spatial patterns of the tropical precipitation and SST responses to Arctic sea ice loss*

Insight into the response of tropical precipitation to Arctic sea ice loss may be gained by examining its spatial pattern in the context of the underlying SST response. Figure 8 shows the simulated climatological rainfall distribution in the tropics and its response to Arctic sea ice loss in ΔICE_coupled. In response to Arctic sea ice loss, the climatological ITCZs in the Pacific shift equatorward and the South Pacific convergence zone (SPCZ) shifts northeastward (cf. Figs. 8a,b). The Atlantic ITCZ also shifts toward the equator, while the Indian Ocean ITCZ, which is located south of the equator in the annual mean, shows a slight strengthening. The equatorward displacements of the Pacific ITCZs in ΔICE_coupled can be understood in the context of the underlying SST response shown in Fig. 8c. Tropical SSTs increase by 0.2°–0.3°C, with maximum warming along the equator in the Pacific sector. Thus, the Pacific ITCZs shift equatorward in response to the altered local meridional SST gradient. A similar relationship between rainfall and SST anomalies is found for ΔRPC8.5 (not shown). The resemblance of the Pacific ITCZ response patterns in ΔICE_coupled (Fig. 8b) and ΔRPC8.5 (Fig. 8d) is noteworthy, although the magnitude of the response to Arctic sea ice loss is only ~15% of that associated with GHG changes.

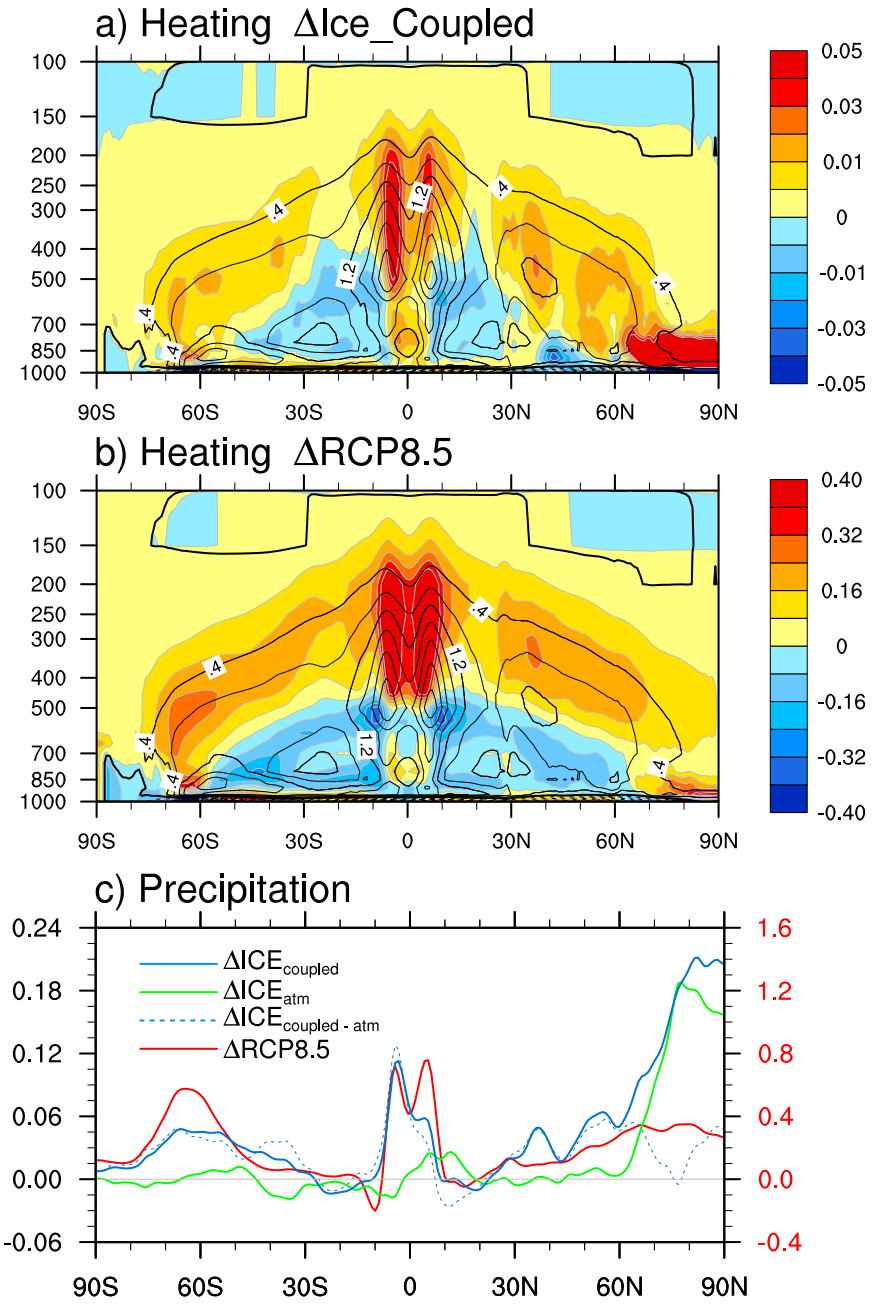

FIG. 7. Annual zonal mean condensational heating rate response (K day^{-1}) in (a) ΔICE_coupled and (b) ΔRCP8.5. Contours show the control (late twentieth century) climatology and shading denotes the response. (c) Annual zonal mean precipitation responses (mm day^{-1}) in ΔICE_coupled (solid blue curve), ΔICE_atm (solid green), and their difference (dotted blue), and in ΔRCP8.5 (red). The left *y* axis is for the blue and green curves, and the right *y* axis is for the red curve.

The seasonal evolution of the zonal mean tropical precipitation responses in ΔICE_coupled and ΔRPC8.5 are shown in Fig. 9 (similar results are found for averages across the Pacific; not shown). Regardless of whether the climatological zonal-mean ITCZ lies in the Northern or Southern Hemisphere, the largest rainfall increase occurs on its equatorward flank in both experiments. The maximum tropical precipitation response in ΔICE_coupled occurs during boreal winter (December–April), consistent with the seasonality of the Arctic

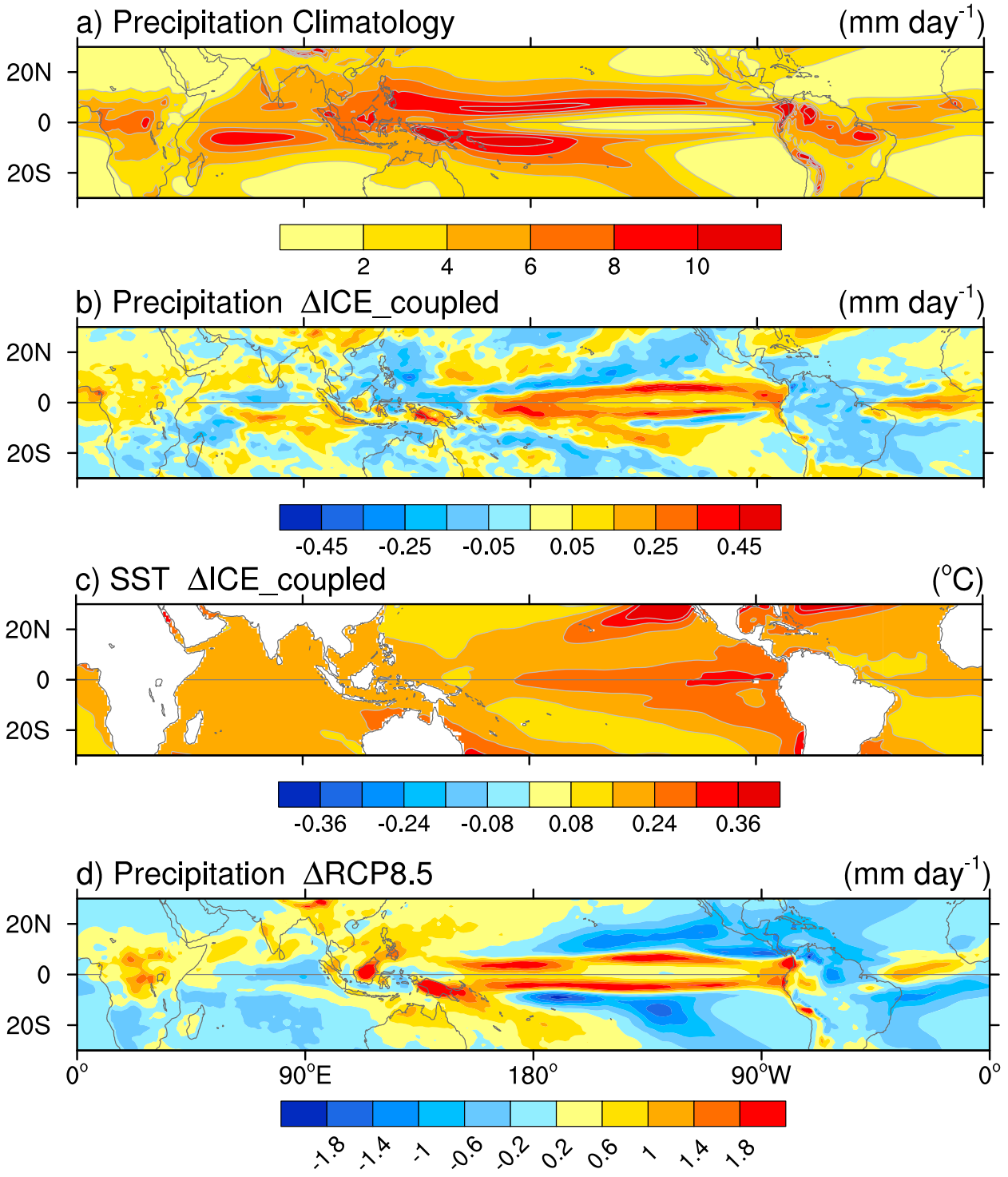

FIG. 8. (a) Annual precipitation climatology from the twentieth-century ICE_coupled_20 run. (b) Annual precipitation response (mm day^{-1}) and (c) SST response (°C) in ΔICE_coupled. (d) Annual precipitation response in ΔRCP8.5. Note the different color scales in (b) and (d).

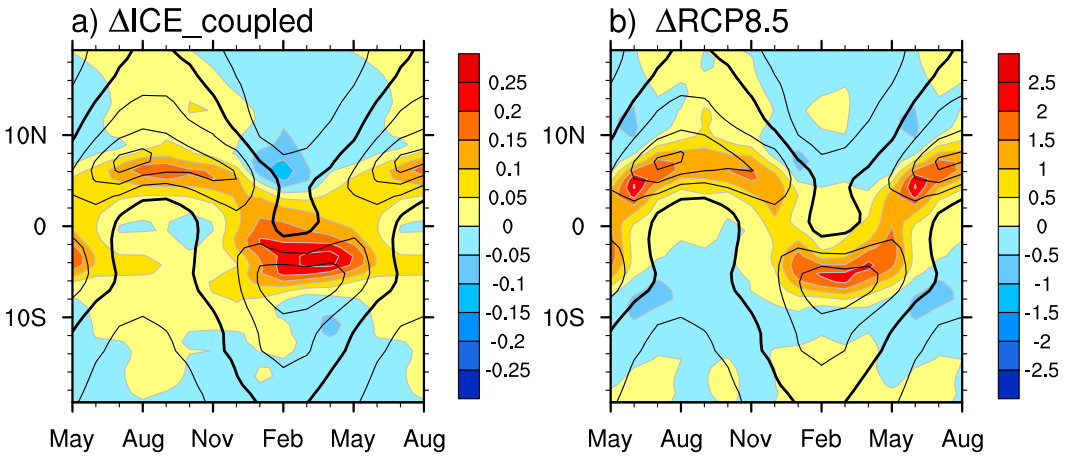

FIG. 9. Monthly zonally averaged tropical precipitation responses (color shading; mm day^{-1}) in (a) ΔICE_coupled and (b) ΔRCP8.5. Contours show the climatological precipitation, with a contour interval of 2 mm day^{-1} and the 4 mm day^{-1} contour is thickened.

surface heat flux response, while the rainfall response in ΔRPC8.5 shows a smaller seasonal dependence. Unlike precipitation, the SST response always peaks at the equator independent of the time of year (not shown).

f. Northward energy transport: Response to Arctic sea ice loss and the role of ocean dynamics

Meridional energy transport plays a fundamental role governing the response of the climate system to an imposed heat source. Here we examine the changes in annual mean northward energy transport (NET) resulting from Arctic sea ice loss in ΔICE_coupled and ΔICE_atm. The atmospheric component of the NET is obtained from the meridional integral of the difference between the zonal mean net top-of-atmosphere radiation and surface energy flux at each latitude. The oceanic component is the vertical and meridional integral of the net surface ocean heat fluxes. Figure 10 shows that NET in both the atmosphere and ocean diminish in response to Arctic sea ice loss, as expected due to the decrease in meridional temperature gradient between the Arctic and lower latitudes (see also Hwang et al. 2011). In the atmosphere, the reduction in NET is confined to high latitudes (40°–80°N) with the largest decrease (−0.20 PW) near the Arctic Circle (67°N) in both ΔICE_atm and ΔICE_coupled. Thus, the atmosphere diverges excess energy associated with sea ice loss out of the polar cap and converges it into middle latitudes (40°–67°N). The reduction in oceanic NET (in ΔICE_coupled) occurs over a much broader range of latitudes, extending from approximately 45°S to 70°N with the largest decrease (−0.25 PW) around 38°N. Thus, the ocean converges the excess energy associated with Arctic sea ice loss into the tropics, farther south than where the atmosphere deposits it. The diminished oceanic NET is associated with a reduction in the strength of the Atlantic meridional overturning circulation (not shown).

We hypothesize that the dynamical ocean response to Arctic sea ice loss, by converging excess heat into the tropics, causes the equatorially symmetric warming of the tropical oceans which in turn leads to the mini global-warming response pattern documented above. To explicitly test this assertion, we compare the NET responses in ΔICE_coupled and ΔICE_som (Fig. 11a). Except for a slight difference in magnitude owing to a small underestimate of the Arctic sea ice loss in ΔICE_som compared to ΔICE_coupled (not shown), the latitudinal profiles of the total NET responses are very similar in the two sets of experiments. However, the transport changes in ΔICE_som are necessarily accomplished entirely by the atmosphere, whereas in ΔICE_coupled they are due to both the atmosphere and the ocean.

That the atmosphere has to accomplish all of the energy transport in the coupled slab-ocean model setting

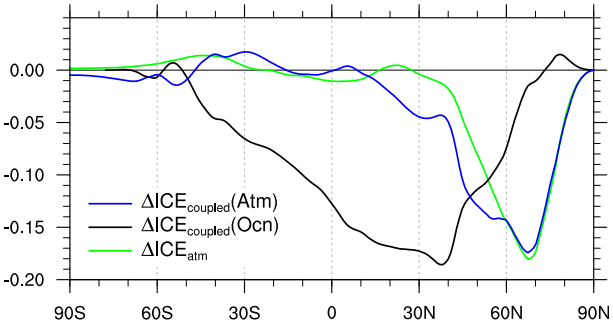

FIG. 10. Annual northward energy transport (PW) response in ΔICE_coupled (blue, atmosphere; black, ocean) and in ΔICE_atm (green, atmosphere).

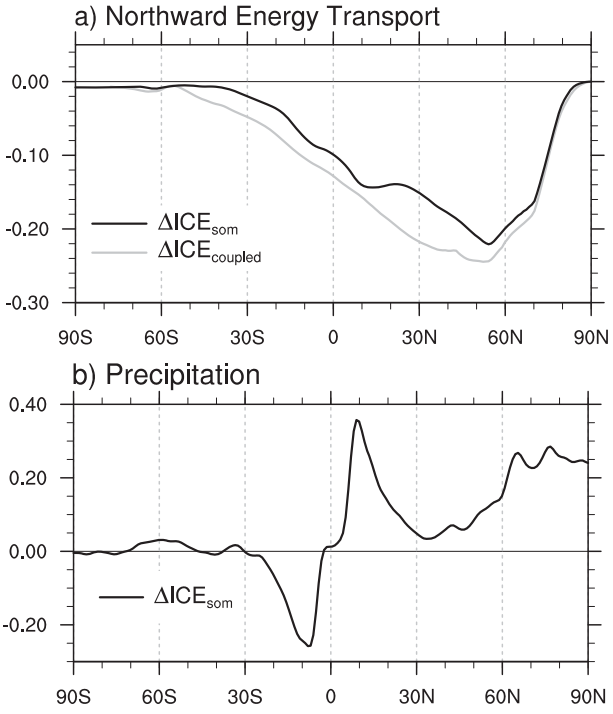

FIG. 11. (a) Annual northward energy transport (PW) response in ΔICE_coupled (sum of the ocean plus atmosphere; gray curve) and ΔICE_som (atmosphere; black curve). (b) Annual precipitation response (mm day^{-1}) in ΔICE_som.

has profound consequences for the global atmospheric response to Arctic sea ice loss. In particular, the tropical precipitation response in ΔICE_som is nearly orthogonal to that in ΔICE_coupled, with increases in rainfall to the north of the equator (maximum values ~ 0.35 mm day^{-1} at 10°N) and decreases to the south of the equator (minimum values ~ -0.25 mm day^{-1} at 10°S; Fig. 11b). In addition, the magnitude of the tropical precipitation response is approximately 3 times larger in ΔICE_som than in ΔICE_coupled. We note that the northward shift of precipitation in the tropics (e.g., toward the warmed NH) in ΔICE_som is energetically consistent with the required reduction in (atmospheric) NET in response to Arctic sea ice loss [e.g., see the arguments put forth in Frierson et al. (2013)], and in agreement with previous studies investigating the response of coupled atmosphere–slab ocean models to extratropical heating anomalies (e.g., Kang et al. 2008; Frierson and Hwang 2012) including Arctic sea ice (CB05). Other aspects of the response in ΔICE_som will be reported in a future study.

4. Summary

We have investigated the role of ocean–atmosphere interaction in the zonal-mean climate response to late twenty-first-century Arctic sea ice loss using the fully coupled CCSM4 model at 1° spatial resolution. To explicitly isolate the contribution of ocean feedbacks, we conducted companion experiments with the atmospheric model component (CAM4) under prescribed sea ice and SST conditions. Additional simulations with the slab ocean version of CCSM4 provided further insight into the roles of dynamic versus thermodynamic ocean coupling in the response to Arctic sea ice loss. Our coupled experiments incorporate a realistic seasonal cycle and spatial pattern of sea ice loss (realistic in the sense that they mimic the ice loss in the CCSM4 RCP8.5 simulation) through the use of a novel longwave radiative nudging technique, enabling a more complete assessment of the role of Arctic sea ice loss in future anthropogenic climate change than previous studies. Our key results may be summarized as follows.

In the absence of ocean coupling, the atmospheric response to Arctic sea ice loss is confined to the northern extratropics, consisting of a weakening and equatorward shift of the westerlies accompanied by lower tropospheric warming and enhanced precipitation at high latitudes, similar to previous atmosphere-only modeling studies (e.g., Deser et al. 2010; Peings and Magnusdottir 2014). With ocean feedbacks, the response expands to cover the whole globe and exhibits a high degree of equatorial symmetry: the entire troposphere warms, the global hydrological cycle strengthens and the ITCZs shift equatorward. This pattern resembles the full response to RCP8.5 radiative forcing with approximately 10%–15% of the amplitude (e.g., a mini global warming). Ocean dynamics are fundamental to producing this equatorially symmetric pattern of response to Arctic sea ice loss: without ocean dynamics, the response takes on an antisymmetric structure. Ocean feedbacks also strengthen the extratropical NH zonal wind response by ~30% in conjunction with enhanced warming of the free troposphere at high latitudes. Finally, the lack of a poleward shift of the wintertime Northern Hemisphere westerlies in CCSM4 under RCP8.5 radiative forcing results from the competing effects of Arctic sea ice loss and greenhouse warming. The magnitudes of the coupled ocean–atmosphere response to Arctic sea ice loss reported here are likely to be conservative due to the 20%–25% underestimate of the winter ice loss in our experiments compared to those in the RCP8.5 scenario.

5. Discussion

The results presented above highlight a number of important issues. The first relates to the seasonal timing of Arctic sea ice loss versus the response of the net surface energy flux. Although the areal extent of late twenty-first-century Arctic sea ice loss is greatest in late

fall–early winter (October–November), the net (upward) surface heat flux response of the Arctic Ocean peaks in midwinter (December–February) in both the uncoupled and coupled experiments. This is due to the contribution of the turbulent energy fluxes, which maximize in winter when the climatological air–sea temperature differences over the Arctic Ocean are greatest. This result has implications for the timing of the atmospheric circulation response, which is forced by the surface energy fluxes rather than by the sea ice directly.

A second related issue concerns the seasonal cycle of the sea ice loss itself. Traditionally, coupled modeling studies have modified the sea ice albedo as a means of reducing ice cover. However, this approach does little to lower sea ice in winter, although it achieves the desired effect in summer. Because of the greater sensitivity of the surface heat flux response to sea ice anomalies in winter compared to other times of year as discussed above, the ice–albedo approach will greatly underestimate the net heat flux forcing associated with Arctic sea ice loss. In CCSM4, the surface heat flux response to projected late twenty-first-century Arctic sea ice loss is underestimated by approximately 80% in winter (~50% in the annual mean) in the modified ice–albedo experiments compared to the longwave-forced simulations (which have a better representation of the full seasonal cycle of projected sea ice loss). Thus, to adequately assess the role of Arctic sea ice loss in the coupled ocean–atmosphere system, an alternative to the traditional ice albedo methodology is needed. In this study, we have introduced a new technique to obtain realistic year-round ice loss by adding a seasonally dependent downward longwave radiative flux to the sea ice model. Although this technique does not conserve energy, water in the ocean and ice models is conserved. This would not be true if the ice distribution were prescribed or nudged directly, potentially resulting in detrimental effects on the climate response.

A third issue relates to the role of ocean coupling in the global climate response to projected Arctic sea ice loss. Modeling studies on the climate impacts of sea ice loss have typically ignored air–sea feedbacks, favoring instead the use of atmospheric models (e.g., Singarayer et al. 2006; Seierstad and Bader 2009; Deser et al. 2010; Liu et al. 2012; Peings and Magnusdottir 2014; and many others), and occasionally incorporating the accompanying warming of Arctic Ocean SSTs (e.g., Screen et al. 2013, 2015). This study shows that ocean–atmosphere coupling modifies the response to projected Arctic sea ice loss in two important ways: 1) the extratropical NH zonal wind response strengthens by ~30% in conjunction with enhanced tropospheric warming at high latitudes, and 2) the temperature, wind, and precipitation responses extend into the tropics and SH, and exhibit a high degree of symmetry about the equator reminiscent of the response to GHG forcing.

In the fully coupled response to Arctic sea ice loss, the enhanced warming of the free troposphere at high latitudes can be traced to an increase in condensational heating that in turn results from greater poleward transport of water vapor compared to the uncoupled response (not shown). This mechanism is consistent with the results of Hwang and Frierson (2010) for the GHG forcing case, and underscores the notion that the coupled ocean–atmosphere response to Arctic sea ice loss resembles a miniature version of the response to GHG forcing. Indeed, we interpret the similarity between the patterns of the global coupled response to Arctic sea ice loss and GHG forcing to result ultimately from the radiative effects associated with their common increase in atmospheric moisture content.

In addition to the global nature of the atmospheric response to Arctic sea ice loss when ocean feedbacks are active, an important finding of this study is the role of Arctic sea ice loss in causing the asymmetry between the northern and southern annular mode responses to GHG forcing. The extratropical NH exhibits a notable lack of a coherent tropospheric zonal wind response to RCP8.5 radiative forcing during the cold season, whereas the SH shows a significant poleward shift of the midlatitude westerlies year-round. Our results demonstrate that Arctic sea ice loss (itself driven by the radiative forcing) is largely responsible for this hemispheric asymmetry. When the effects of Arctic sea ice loss are accounted for, the NH westerlies respond in a similar fashion as the SH westerlies, with a continuous and significant poleward shift throughout the year. This result offers a simple explanation for the hemispheric asymmetries in the annular mode response to GHG forcing, and confirms the empirical study of Cattiaux and Cassou (2013), who found a strong (inverse) relationship between the magnitudes of projected Arctic sea ice loss and NAM response in the CMIP phases 3 and 5 archives. It also agrees with the results of Sigmond and Scinocca (2010) based on simplified dynamical atmospheric model experiments forced with GHG increases in the absence of sea ice changes.

The tropical precipitation and SST responses to Arctic sea ice loss in our fully coupled experiments merit additional discussion, given that they differ from those of earlier studies (e.g., CB05). Rather than shifting toward the Arctic (e.g., toward the hemisphere with the anomalous atmospheric heating), the ITCZs intensify on their equatorward flanks in association with an increase in tropical SSTs and maximum warming along the equator, especially in the Pacific. Thus, the local control of the SST warming pattern seems to play a larger role in the

tropical rainfall response than the remote control of the Arctic heating. Dynamical ocean processes produce the equatorial SST anomaly maximum, with air–sea energy fluxes acting to damp it (not shown). Coupled model experiments employing a thermodynamic slab ocean mixed layer necessarily lack this dynamically induced mechanism of tropical response to Arctic sea ice loss. Indeed, CB05 found that in their coupled atmosphere-slab ocean model simulations, the ITCZ shifts southward in response to increased Northern Hemisphere sea ice cover. Our slab-ocean model experiments confirm the results of CB05 (in our case, a northward shift of the ITCZ in response to diminished Arctic sea ice). Thus, our study highlights the transformative role of ocean dynamics in the global response to Arctic sea ice loss.

The distinction between the structures of the tropical response in coupled models with a slab ocean versus a dynamical ocean is also evident for radiative forcing in the middle latitudes. For example, idealized coupled slab ocean model experiments show a meridional shift of the ITCZ toward the hemisphere in which an extratropical heat source has been imposed (Kang et al. 2008, 2009). On the other hand, coupled dynamical ocean models show an equatorially symmetric response of the ITCZ to aerosol forcing that peaks in the NH midlatitudes, similar in structure (but of opposite sign) to that produced by GHG forcing (Xie et al. 2013). The general issue of the role of ocean dynamics in the sensitivity of tropical SST and rainfall response patterns to mid- and high-latitude forcing warrants further investigation.

This study has focused on the equilibrium response of the coupled ocean–atmosphere system to Arctic sea ice loss. The mechanisms and pathways of the transient adjustment process, including the roles of the MOC and wind–evaporation–SST feedback (Liu and Xie 1994; Vimont 2010) in communicating the signal from the Arctic to the global oceans, are left to future work.

Acknowledgments. This work was supported by a grant from the Office of Polar Programs at the National Science Foundation. We thank Laura Landrum (NCAR) for conducting the modified sea ice albedo experiment. We appreciate the constructive comments and suggestions from the three reviewers and editor John Walsh.

APPENDIX

Formulation of the Coupled Model Experiments with Constrained Sea Ice

The following description is for the case of deriving the longwave radiative flux (LRF) for a late twenty-first-century coupled sea ice experiment. Similar methodology was used for the late twentieth-century coupled sea ice control, with negative rather than positive values of LRF. Our objective was to produce a file containing monthly and spatially varying fields of longwave radiation to force the sea ice model. New code was written for the sea ice model to read the appropriate months from this file and linearly interpolate the data to model time as the simulation was running. A monthly varying mask was first constructed to specify the spatial distribution of the long LRF. The mask was obtained by taking the difference between the monthly sea ice concentrations from the late twenty-first-century RCP8.5 ensemble mean minus the late twentieth-century historical ensemble mean. If there was a decrease exceeding a threshold of −10% in a grid cell, LRF was added to that cell; otherwise, no forcing was used at that location. Next, an ensemble of four experiments was performed using the monthly varying mask with time invariant LRF of 0, 10, 20, and 30 $\mathrm{W\,m^{-2}}$. Each simulation was then run for 30 years. The area averaged sea ice concentration in these

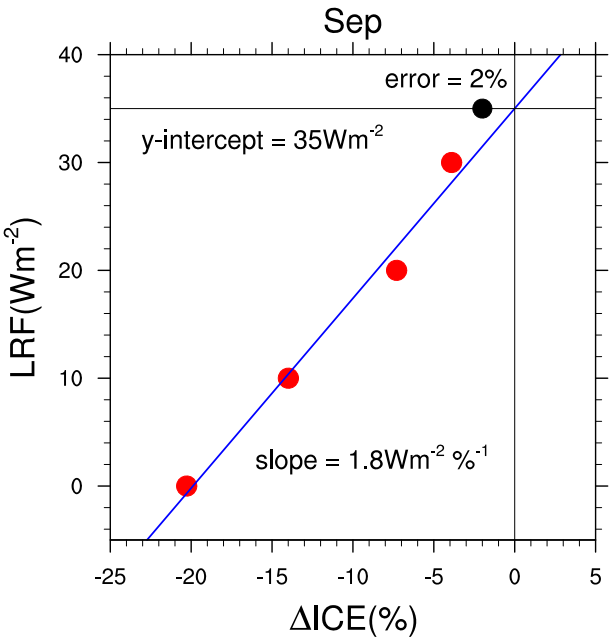

FIG. A1. Scatterplot of the longwave radiative forcing (LRF) in each of the four initial experiments vs the difference in area average sea ice concentration, late twenty-first-century RCP8.5 minus LRF experiments (red circles) and the linear least squares fit to the data (blue line). The black circle indicates the area average sea ice concentration from the last 30 yr of a 100-yr simulation made using monthly LRF magnitude derived from the monthly *y*-intercept values. This illustrative example is from a late twenty-first-century sea ice simulation using the Whole Atmosphere Community Climate Model (WACCM), conducted after the experiments discussed in this study. Using the WACCM simulation allows us to illustrate all steps and refinements that went into the final methodology, which provided the closest match to the target sea ice.

TABLE A1. LRF ($W m^{-2}$) by month for the twenty-first- and twentieth-century coupled ice simulations (ICE_coupled_20 and ICE_coupled_21, respectively) obtained by following the procedure described in the appendix.

	Jan	Feb	Mar	Apr	May	Jun	Jul	Aug	Sep	Oct	Nov	Dec
Twenty-first century	184	114	82	58	54	49	61	48	53	113	159	104
Twentieth century	−23	−25	−24	−21	−12	−7	−5	−4	−4	−5	−8	−14

simulations came into equilibrium after approximately 10 years and the last 20 years were analyzed. The differences, calculated by subtracting the monthly area averaged sea ice concentration from the late twenty-first-century RCP8.5 (i.e., the target ice) minus the monthly area averages from each ensemble member were plotted as a function of the four values of LRF used for each ensemble member. An example for the month of September is shown in Fig. A1 (red circle) along with the linear least squares fit line (blue line). Note that the data in Fig. A1 display a mostly linear relationship and this was also the case during the months from early summer through early winter. During midwinter through late spring, there was more spread in the data (not shown). This seasonal difference appears to be consistent with our ability to match the sea ice loss (Fig. 3a). The y intercept in the scatterplots provides an estimate of the monthly forcing that should result in zero difference between the late twenty-first-century RCP8.5 and LRF experiments ($35 W m^{-2}$ in Fig. A1). An adjustment was applied to the y-intercept numbers to create the forcing file because the sea ice model code linearly interpolates in time between the 12 values in the forcing file and the monthly average of these interpolated values is not the same as the monthly y intercepts. This procedure is identical to the adjustment procedure used to produce SST boundary forcing for AMIP simulations and is described in Taylor et al. (2000).

After running a simulation for approximately 100 yr using the LRF derived as described in the preceding paragraphs, the sea ice concentration can be evaluated and an adjustment made. The area averaged sea ice concentration from years 70–100 from such a simulation is indicated by the black marker in Fig. A1. The adjustment makes use of the error, defined as the difference between the sea ice concentration in the late twenty-first-century RCP8.5 experiments minus the century-long LRF experiment, and the slope of the least squares fit line, using the formula $LRF_{adjusted} = LRF - (slope \times error)$. In Fig. A1, $LRF = 35.0 W m^{-2}$, the slope is $1.8 W m^{-2} (\%)^{-1}$ and the error is -2.0%, yielding $LRF_{adjusted} = 36.6 W m^{-2}$. We developed this adjustment procedure while producing our twentieth-century coupled control, and after completing our twenty-first-century coupled simulation. We did not go back and adjust our twenty-first-century simulation using this methodology, however, because the monthly sea ice concentrations without the adjustment were felt to be sufficiently close for our purposes and the additional time and expense was not warranted. LRF values for the twenty-first- and twentieth-century coupled ice experiments are listed in Table A1.

REFERENCES

Barnes, E. A., 2013: Revisiting the evidence linking Arctic amplification to extreme weather in midlatitudes. *Geophys. Res. Lett.,* **40,** 4728–4733, doi:10.1002/grl.50880.

Bitz, C. M., K. M. Shell, P. R. Gent, D. A. Bailey, G. Danabasoglu, K. C. Armour, M. M. Holland, and J. T. Kiehl, 2012: Climate sensitivity of the Community Climate System Model version 4. *J. Climate,* **25,** 3053–3070, doi:10.1175/JCLI-D-11-00290.1.

Briegleb, B. P. and B. Light, 2007: A Delta-Eddington multiple scattering parameterization for solar radiation in the sea ice component of the Community Climate System Model. NCAR Tech. Note NCAR/TN-472+STR, 100 pp, doi:10.5065/D6B27S71.

Cattiaux, J., and C. Cassou, 2013: Opposite CMIP3/CMIP5 trends in the wintertime Northern Annular Mode explained by combined local sea ice and remote tropical influences. *Geophys. Res. Lett.,* **40,** 3682–3687, doi:10.1002/grl.50643.

Chiang, J. C. H., and C. M. Bitz, 2005: Influence of high latitude ice on the marine Intertropical Convergence Zone. *Climate Dyn.,* **25,** 477–496, doi:10.1007/s00382-005-0040-5.

Deser, C., R. Tomas, M. Alexander, and D. Lawrence, 2010: The seasonal atmospheric response to projected Arctic sea ice loss in the late twenty-first century. *J. Climate,* **23,** 333–351, doi:10.1175/2009JCLI3053.1.

Francis, J., and S. Vavrus, 2012: Evidence linking Arctic amplification to extreme weather in mid-latitudes. *Geophys. Res. Lett.,* **39,** L06801, doi:10.1029/2012GL051000.

Frierson, D. M. W., and Y.-T. Hwang, 2012: Extratropical influence on ITCZ shifts in slab ocean simulations of global warming. *J. Climate,* **25,** 720–733, doi:10.1175/JCLI-D-11-00116.1.

——, and Coauthors, 2013: Contribution of ocean overturning circulation to tropical rainfall peak in the Northern Hemisphere. *Nat. Geosci.,* **6,** 940–944, doi:10.1038/ngeo1987.

Gent, P., and Coauthors, 2011: The Community Climate System Model version 4. *J. Climate,* **24,** 4973–4991, doi:10.1175/2011JCLI4083.1.

Graversen, R. G., and M. Wang, 2009: Polar amplification in a coupled climate model with locked albedo. *Climate Dyn.,* **33,** 629–643, doi:10.1007/s00382-009-0535-6.

Holland, M. M., D. A. Bailey, B. P. Briegleb, B. Light, and E. Hunke, 2012: Improved sea ice shortwave radiation physics in CCSM4: The impact of melt ponds and black carbon. *J. Climate,* **25,** 1413–1430, doi:10.1175/JCLI-D-11-00078.1.

Hwang, Y.-T., and D. M. W. Frierson, 2010: Increasing atmospheric poleward energy transport with global warming. *Geophys. Res. Lett.,* **37,** L24807, doi:10.1029/2010GL045440.

——, ——, and J. E. Kay, 2011: Coupling between Arctic feedbacks and changes in poleward energy transport. *Geophys. Res. Lett.,* **38,** L17704, doi:10.1029/2011GL048546.

Jahn, A., and Coauthors, 2012: Late-twentieth-century simulation of Arctic sea ice and ocean properties in the CCSM4. *J. Climate,* **25,** 1431–1452, doi:10.1175/JCLI-D-11-00201.1.

Kang, S. M., I. M. Held, D. M. W. Frierson, and M. Zhao, 2008: The response of the ITCZ to extratropical thermal forcing: Idealized slab-ocean experiments with a GCM. *J. Climate,* **21,** 3521–3532, doi:10.1175/2007JCLI2146.1.

——, D. M. W. Frierson, and I. M. Held, 2009: The tropical response to extratropical thermal forcing in an idealized GCM: The importance of radiative feedbacks and convective parameterization. *J. Atmos. Sci.,* **66,** 2812–2827, doi:10.1175/2009JAS2924.1.

Kay, J. E., M. M. Holland, and A. Jahn, 2011: Inter-annual to multi-decadal Arctic sea ice extent trends in a warming world. *Geophys. Res. Lett.,* **38,** L15708, doi:10.1029/2011GL048008.

Liu, J., J. Curry, H. Wang, M. Song, and R. Horton, 2012: Impact of declining Arctic sea ice on winter snowfall. *Proc. Natl. Acad. Sci. USA,* **109,** 4074–4079, doi:10.1073/pnas.1114910109.

Liu, Z., and S. Xie, 1994: Equatorward propagation of coupled air–sea disturbances with application to the annual cycle of the eastern tropical Pacific. *J. Atmos. Sci.,* **51,** 3807–3822, doi:10.1175/1520-0469(1994)051<3807:EPOCAD>2.0.CO;2.

Peings, Y., and G. Magnusdottir, 2014: Response of the wintertime Northern Hemisphere atmospheric circulation to current and projected Arctic sea ice decline: A numerical study with CAM5. *J. Climate,* **27,** 244–264, doi:10.1175/JCLI-D-13-00272.1.

Rind, D., R. Healy, C. Parkinson, and D. Martinson, 1995: The role of sea ice in $2\times CO_2$ climate model sensitivity. Part I: The total influence of sea ice thickness and extent. *J. Climate,* **8,** 449–463, doi:10.1175/1520-0442(1995)008<0449:TROSII>2.0.CO;2.

Scinocca, J., M. Reader, D. Plummer, M. Sigmond, P. Kushner, T. G. Shepherd, and R. Ravishankara, 2009: Impact of sudden Arctic sea-ice loss on stratospheric polar ozone recovery. *Geophys. Res. Lett.,* **36,** L24701, doi:10.1029/2009GL041239.

Screen, J. A., and I. Simmonds, 2010: Increasing fall–winter energy loss from the Arctic Ocean and its role in Arctic temperature amplification. *Geophys. Res. Lett.,* **37,** L16797, doi:10.1029/2010GL044136.

——, and ——, 2013: Exploring links between Arctic amplification and mid-latitude weather. *Geophys. Res. Lett.,* **40,** 959–964, doi:10.1002/grl.50174.

——, ——, C. Deser, and R. Tomas, 2013: The atmospheric response to three decades of observed Arctic sea ice loss. *J. Climate,* **26,** 1230–1248, doi:10.1175/JCLI-D-12-00063.1.

——, C. Deser, and L. Sun, 2015: Reduced risk of North American cold extremes due to continued sea ice loss. *Bull. Amer. Meteor. Soc.,* doi:10.1175/BAMS-D-14-00185.1, in press.

Seierstad, I. A., and J. Bader, 2009: Impact of a projected future Arctic sea ice reduction on extratropical storminess and the NAO. *Climate Dyn.,* **33,** 937–943, doi:10.1007/s00382-008-0463-x.

Serreze, M. C., and R. G. Barry, 2011: Processes and impacts of Arctic amplification: A research synthesis. *Global Planet. Change,* **77,** 85–96, doi:10.1016/j.gloplacha.2011.03.004.

Sigmond, M., and J. F. Scinocca, 2010: The influence of the basic state on the Northern Hemisphere circulation response to climate change. *J. Climate,* **23,** 1434–1446, doi:10.1175/2009JCLI3167.1.

Singarayer, J. S., J. L. Bamber, and P. J. Valdes, 2006: Twenty-first-century climate impacts from a declining Arctic sea ice cover. *J. Climate,* **19,** 1109–1125, doi:10.1175/JCLI3649.1.

Stocker, T. F., and Coauthors, Eds., 2013: *Climate Change 2013: The Physical Science Basis.* Cambridge University Press, 1535 pp.

Stroeve, J. C., V. Kattsov, A. Barrett, M. Serreze, T. Pavlova, M. Holland, and W. N. Meier, 2012: Trends in Arctic sea ice extent from CMIP5, CMIP3 and observations. *Geophys. Res. Lett.,* **39,** L16502, doi:10.1029/2012GL052676.

Taylor, K. E., D. Williamson, and F. Zwiers, 2000: The sea surface temperature and sea-ice concentration boundary conditions for AMIP II simulations. PCMDI Rep. 60 and UCRL-MI-125597, Lawrence Livermore National Laboratory, 25 pp. [Available online at http://www-pcmdi.llnl.gov/publications/ab60.html.]

——, R. J. Stouffer, and G. Meehl, 2012: An overview of CMIP5 and the experiment design. *Bull. Amer. Meteor. Soc.,* **93,** 485–498, doi:10.1175/BAMS-D-11-00094.1.

Vimont, D. J., 2010: Transient growth of thermodynamically coupled disturbances in the tropics under an equatorially symmetric mean state. *J. Climate,* **23,** 5771–5789, doi:10.1175/2010JCLI3532.1.

Wettstein, J. J., and C. Deser, 2014: Internal variability in projections of twenty-first century Arctic sea ice loss: Role of the large-scale atmospheric circulation. *J. Climate,* **27,** 527–550, doi:10.1175/JCLI-D-12-00839.1.

Xie, S.-P., B. Lu, and B. Xiang, 2013: Similar spatial patterns of climate responses to aerosol and greenhouse gas changes. *Nat. Geosci.,* **6,** 828–832, doi:10.1038/ngeo1931.